

# Calibration of the CAT Telescope

Frédéric Piron, for the CAT collaboration

*Laboratoire de Physique Nucléaire des Hautes Energies  
Ecole Polytechnique, route de Saclay, 91128 Palaiseau Cedex, France*

**Abstract.** Due to the lack of test-beams in ground-based  $\gamma$ -ray astronomy, detector calibration has been a major challenge in this field. However, with the use of Cherenkov ring-images due to cosmic-ray muons and of strong  $\gamma$ -ray signals, the CAT telescope could be rather well monitored and understood. Here we present a few outstanding aspects of this work.

## INTRODUCTION: THE CAT DETECTOR

The CAT (Cherenkov Array at Thémis) telescope records Cherenkov flashes due to VHE atmospheric showers through its 17.8m<sup>2</sup> mirror. Its camera is located 6m from the mirror and has a 4.8° full field of view, consisting of a central region of 546 0.12° angular diameter phototubes arranged in a hexagonal matrix and of 54 surrounding tubes in two “guard rings” (Fig.1a). Fast electronics allows a relatively low  $\gamma$ -ray detection threshold energy of 250 GeV (at Zenith), and the fine grain of the camera permits an accurate image analysis. The experiment and the analysis method are fully described elsewhere [1,5]. Briefly, after selecting the most significant triggers (total charge  $Q_{\text{tot}} > 30$  photo-electrons), good discrimination between  $\gamma$  and hadron-induced showers is achieved by looking at the shape and the orientation of the images (see the events on Fig. 1a): since  $\gamma$ -ray images are rather thin and ellipsoidal while hadronic images are more irregular, a first cut is applied which selects images with a “ $\gamma$ -like” shape; it is based on a  $\chi^2$  fit to a mean light distribution predicted from electromagnetic showers, and a probability  $P(\chi^2) > 0.35$  is required. Then, since  $\gamma$ -ray images are expected to point towards the source position in the focal plane whereas cosmic-ray directions are isotropic, a second cut  $\alpha < 6^\circ$  is used in the case of a point-like source, where the pointing angle  $\alpha$  is defined as the angle at the image barycentre between the actual source position in the focal plane and that of the image which is reconstructed by the fit <sup>1</sup>. As a result, this procedure rejects 99.5% of hadronic events while selecting 40% of  $\gamma$ -ray events. Fig 1b is an example of the pointing angle distribution obtained on the Crab nebula: the signal is clearly seen in the first bins, while a second signal can be

---

<sup>1</sup>) The resolution per event is of the order of the pixel size, i.e.  $\sim 0.1^\circ$ .

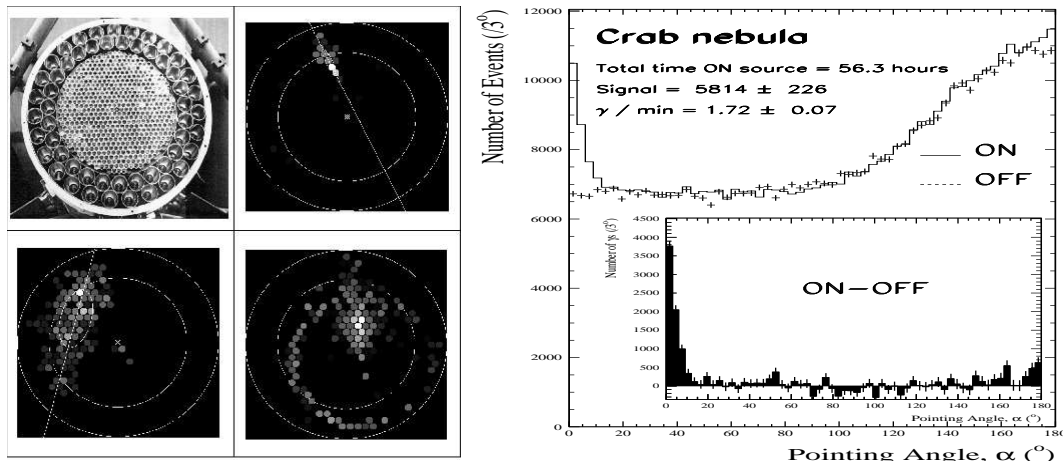


**FIGURE 1.** (a) The CAT camera and three typical events: the first image is presumably due to a  $\gamma$  shower because of its fine and cometary shape, and because it is pointing towards the source position at the center of the camera; the second image is certainly due to a hadron because it is more spread out and pointing elsewhere; finally, the third image is clearly hadronic and would be easily rejected, because it is signed by the presence of a muon ring. (b) Pointing angle distribution from a sample of data taken on the Crab nebula between 1996 and 1999, for zenith angles ranging from  $21^\circ$  to  $35^\circ$ . Cuts on total charge and shape have been applied (see text). The inset shows the ON–OFF distribution (OFF source runs are used to estimate the hadronic background): within  $6^\circ$ , the total significance is  $25.6\sigma$  for a ratio of durations  $T_{\text{ON}}/T_{\text{OFF}} = 2.4$  (the OFF distribution has been renormalized). The corresponding significance for an equal amount of ON and OFF runs would be  $32.2\sigma$ , i.e.  $4.3\sigma$  in one hour.

seen at  $\alpha \sim 180^\circ$ , due to  $\gamma$ -ray images whose direction has been mis-reconstructed by the fit <sup>2</sup>.

## CALIBRATION OF THE DETECTOR

### Hardware monitoring

Mrk 501 exhibited a remarkable series of flares during the whole year 1997 [3], which have been very useful for detector calibration. As an example, Fig. 2a illustrates the very good quality of the mechanical monitoring for data taken with a zenith angle between  $0^\circ$  and  $44^\circ$ : the signal appears right at the actual position of the source, thus validating the angular correction which is applied on each event to compensate for the unavoidable and zenith-dependent slight mis-alignment of the optical axis of the camera <sup>3</sup>.

<sup>2</sup>) The global rise of the background distribution for large values of  $\alpha$  corresponds to large hadronic images which were cut by the edge of the camera. This effect becomes fainter for larger zenith angles, since images form closer to the center of the camera; see [6] for illustration.

<sup>3</sup>) This is due to the weight of the camera, which bends the arms of the telescope, and to the telescope azimuth and altitude axis mis-alignment, especially at large zenith angles.

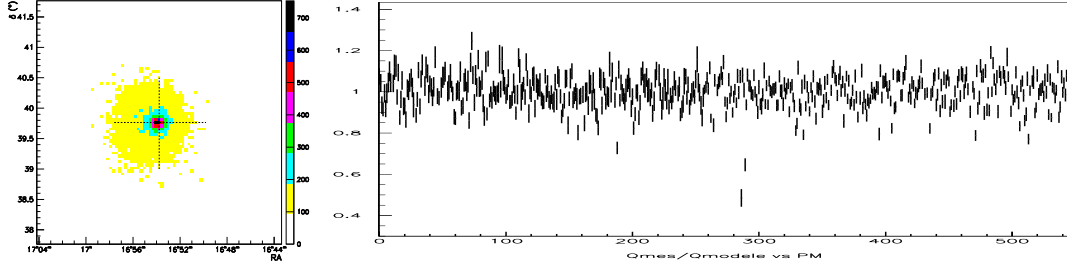


**FIGURE 2.** (a) Projected distribution (bin size= $0.05^\circ$ ) of the reconstructed shower angular origins for all data of Mrk 501 in 1997: no background subtraction has been performed, and events are selected by the shape cut only. The cross marks the actual position of Mrk 501. (b) Ratio of the charge integrated in each of the 546 small inner phototubes to that predicted by a model of muon rings.  $\sim 100$  muon images have been used for these statistics. The dispersion of the ratio around unity is mainly due to the uncertainty on the gain values.

Cosmic-ray muons falling onto the mirror yield ring-like images in which the light distribution can be easily predicted. The fine grain of the CAT camera allows a fine analysis of these images [4]. In this way, the overall conversion factor between ADC counts and incident Cherenkov photon number can be directly checked. This factor involves optical efficiencies, as well as phototube pedestals and gains. As an example, Fig 2b shows that the camera is correctly calibrated, except for a few channels which are not used in the analysis. In this study, particular attention has been paid to the wavelength-dependent aspect, by taking special runs using different UV-filters placed in front of the camera.

## Validation of the simulations

On April 16<sup>th</sup>, 1997, Mrk 501 reached  $\sim 8$  times the level of the Crab nebula. The signal-to-noise ratio for this night is 2.7, corresponding to a  $\gamma$ -ray beam with only 30% contamination. The good atmospheric quality of this night allows the use of this beam for calibration through comparison with simulations. Fig. 3a shows the perfect agreement on the distributions of Hillas parameters [7]: it is shown for events selected both with the single orientation cut and with the complete selection including the  $\chi^2$  fit. The distribution of the final number of pixels  $N^{\text{pix}}$  retained by the fit (see [5]) is also well reproduced. Furthermore, the good agreement observed on the fourth-brightest-pixel's charge  $Q^{4\text{th}}$  validates the simulations at the trigger level, since the trigger condition requires four pixels above threshold. Finally, Fig. 3b shows the  $\chi^2/\text{ndf}$  and  $P(\chi^2)$  distributions <sup>4</sup>, as well as the previously discussed parameters, expressed as functions of the total image charge  $Q_{\text{tot}}$ : here again the agreement is very good. This allows the simulation to be used to calculate

<sup>4</sup>) The  $P(\chi^2)$  distribution is not flat, as would be expected if the  $\chi^2$  were performed using variables with Gaussian errors. The description of Cherenkov light fluctuations in showers development is a very difficult task (see [5] for discussion).

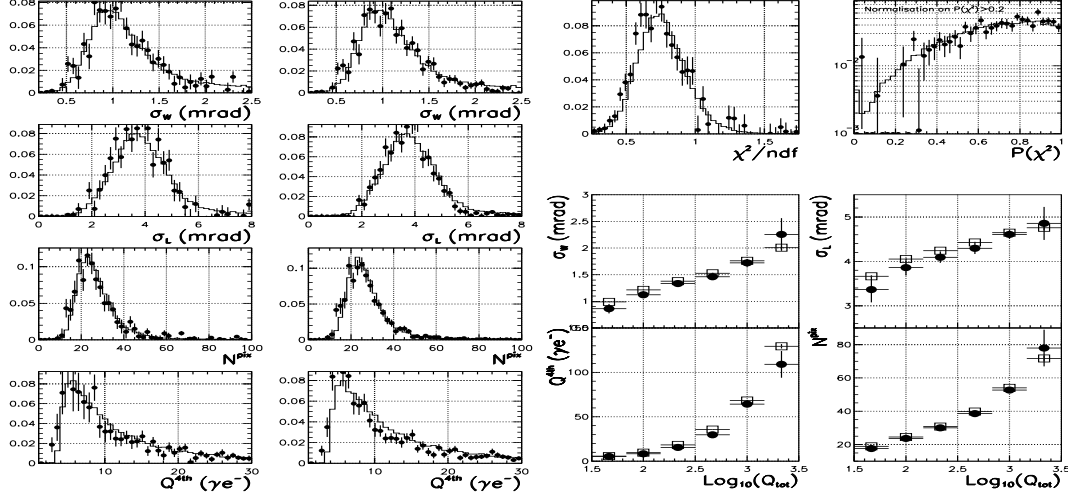


**FIGURE 3.** Comparison of  $\gamma$ -ray shower simulations (full lines or open squares) with the data (ON–OFF) from the flare of Mrk 501 on April 16<sup>th</sup>, 1997 (filled points). Statistical errors are negligible for simulations. (a) Distribution of several variables, within the orientation cut  $\alpha < 6^\circ$  (left column) and with the cut on shape  $P(\chi^2) > 0.35$  also (right column): Hillas parameters *width* ( $\sigma_W$ ) and *length* ( $\sigma_L$ ), number of pixels in the image  $N^{\text{pix}}$ , and fourth-brightest-pixel's charge  $Q^{4\text{th}}$ ; (b)  $\chi^2/\text{ndf}$  and  $P(\chi^2)$  distributions, and previous parameters as functions of  $\text{Log}_{10}(Q_{\text{tot}})$ .

the  $\gamma$ -ray effective detection area within the selection cuts, as well as the energy-resolution function  $\Psi$ . This is shown in Fig. 4. In particular, a clear positive bias in the energy reconstruction is visible for low values of the injected energy (Fig. 4b):

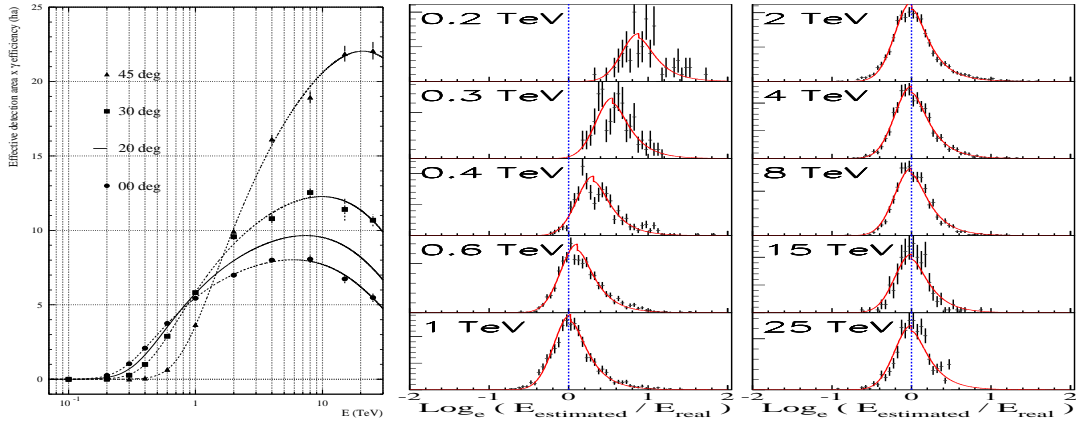


**FIGURE 4.** (a)  $\gamma$ -ray effective detection area (in  $10^4 \text{m}^2$ ), including the effect of event-selection efficiency, as a function of the energy. Each point corresponds to simulations, while full lines come from an analytical 2D-interpolation over energy and zenith angle; (b) Energy-resolution functions  $\Psi(E \rightarrow \tilde{E}, \cos\theta)$  vs  $\log(\tilde{E}/E)$ , for a fixed zenith angle  $\theta = 30^\circ$  ( $y$ -axis units are arbitrary). Each plot is defined for a fixed value of the *real* energy  $E$ , ranging from 200 GeV to 25 TeV, and runs on the *estimated* energy  $\tilde{E}$ . Full lines come from an analytical 3D-interpolation over the three variables  $E$ ,  $\tilde{E}$  and  $\theta$ .

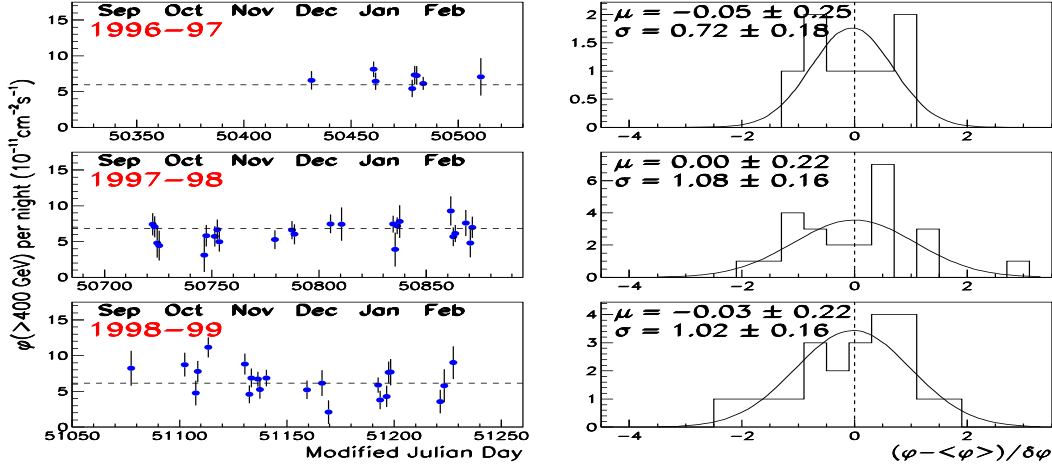


**FIGURE 5.** 1996 to 1999 nightly integral flux of the Crab nebula above 400 GeV, from a sample of data with zenith angles up to  $35^\circ$ . The dotted lines represents the mean flux for each period, and the corresponding residuals are shown on the right panel.

it is due to a trigger effect which selects those events which benefited from a positive fluctuation of Cherenkov light during the shower development. This energy over-estimation disappears when going towards higher energies, where  $\Psi$  becomes more Gaussian, with a zero mean value and a width  $\sigma \sim 20\%$ .

## CONCLUSION

More details concerning calibration and spectrum measurement will be given in a forthcoming paper. The good stability obtained to date on the signal from the Crab nebula (Fig. 5), using the acceptances and energy-resolution function discussed above, illustrates the good quality of running conditions and the good understanding of the detector. Future effort will be devoted to the analysis of large zenith angle data (see [6] for a first study) and to the cross-calibration with the CELESTE experiment, operating on the same site with an energy threshold of  $\sim 50$  GeV; the recent observation of the first common events between both detectors [2] is an encouraging result in this direction.

## REFERENCES

1. Barrau, A., *et al*, *Nucl. Instr. Meth. A* **416**, 278 (1998).
2. De Naurois, M., *et al*, *Proc. XXVI ICRC* **5**, 211 (Salt-Lake City, 1999).
3. Djannati-Ataï, A., *et al*, *A&A* **350**, 17 (1999).
4. Iacoucci, L., *Ph.D. thesis*, Ecole Polytechnique, Palaiseau, France (1998).
5. Le Bohec, S., *et al*, *Nucl. Instr. Meth. A* **416**, 425 (1998).
6. Mohanty, G., *et al*, *Proc. XXVI ICRC* **3**, 452 (Salt-Lake City, 1999).
7. Weekes, T.C., *et al*, *ApJ* **342**, 379 (1989).